

## Rotary Velocity Spectra from Short Drifter Tracks

W. R. CRAWFORD, J. Y. CHERNIAWSKY, AND M. G. G. FOREMAN

*Fisheries and Oceans Canada, Institute of Ocean Sciences, Sidney, British Columbia, Canada*

(Manuscript received 26 August 1996, in final form 28 July 1997)

### ABSTRACT

The authors describe a method utilizing short-duration drifter tracks to compute rotary velocity amplitudes and phases for tidal frequency bands. These are compared to amplitudes and phases from a tidal model, revealing the regions where strong internal tides dominate the observed record or the times when inertial motions compete with the tidal signals. This method therefore enables a direct comparison between Lagrangian drifter data and Eulerian model simulations, while providing information on possible origin and spatial variability of tidal currents.

### 1. Introduction

We describe techniques that permit ocean surface drifter data to be used in the investigation of spatial variability of tidal currents and the comparison of numerical model predictions of these currents in coastal waters. Surface drifters are not usually associated with tidal current analysis, as the latter typically requires relatively long (on the order of weeks and longer) time series at a fixed location in order to resolve individual constituents that have nearly the same frequencies. For example, the semidiurnal M2 and N2 tidal constituents typically require at least 28 days of data for an unambiguous analysis, and the diurnal K1 and P1 constituents require about 6 months of data.

Moreover, drifters usually pass through a coastal region in about a week and seldom stay more than a few days in a region where the tidal currents are uniform (e.g., Thomson et al. 1997). Therefore, the main requirement of statistical analysis, stationarity, is not upheld by drifter data. Nevertheless, ocean surface drifters offer other advantages to coastal current studies. Drifters are relatively cheap and are readily deployed in shipping channels and on fishing banks, where the loss of a few drifters to such traffic would not disturb a survey. Modern drifters may weigh only a few kilograms and pose no threat to vessels. With real-time satellite-transmitting data links, the data recorded up to the time of vessel-induced damage are available and useful.

As a result of these considerations, we now use drifters extensively to study near-surface currents in British Columbia coastal waters. Over the past decade, we have undertaken annual, intensive studies of coastal currents

using Loran C drifters, which are retrieved and redeployed several times during a single survey (Crawford et al. 1995). Figure 1 displays tracks of such deployments in Dixon Entrance and in Hecate Strait, along the northern British Columbia coast in the summer of 1991.

However, we had not previously applied drifter data when evaluating tidal models of this region. Such models (e.g., Foreman et al. 1993; Ballantyne et al. 1996; Cummins and Oey 1997) have relied upon moored current meter observations for evaluation.

In the following two sections, we describe an analysis technique that was specifically designed to identify tidal velocity signals from short duration (1–6 days) drifter track segments. Drifter tidal velocities are then compared to a numerical model output. Using rotary spectral analysis, we identify and map locations of internal tides. These are not usually simulated by the models. We present two examples: (a) a region of strong internal semidiurnal tidal currents and (b) a time of significant inertial-period currents.

### 2. Analysis method

Loran C drifters are described by Crawford (1988) and Woodward et al. (1991). They have a cylindrical, 5-m-high and 1-m-wide drogue, suspended at either a 3- or 10-m depth (middrogue point). Drifter positions were recorded every half-hour on the half-hour. Typical records are from 2 to 20 days long.

To calculate hourly velocities, we extracted the drifter positions at 30 min after each hour, computed the average velocity between these two positions, and assigned it to the position of the drifter on the hour. Each data point in the resulting time series then contained the date, time, latitude, longitude, eastward speed ( $u$ ), and northward speed ( $v$ ). The relative accuracy of Loran C positions is about 25 m rms. This results in rms velocity errors of about 1 cm s<sup>-1</sup>.

---

*Corresponding author address:* Dr. William Crawford, Institute of Ocean Sciences, P.O. Box 6000, Sidney, BC V8L 4B2, Canada.  
E-mail: crawford@dfo-mpo.gc.ca

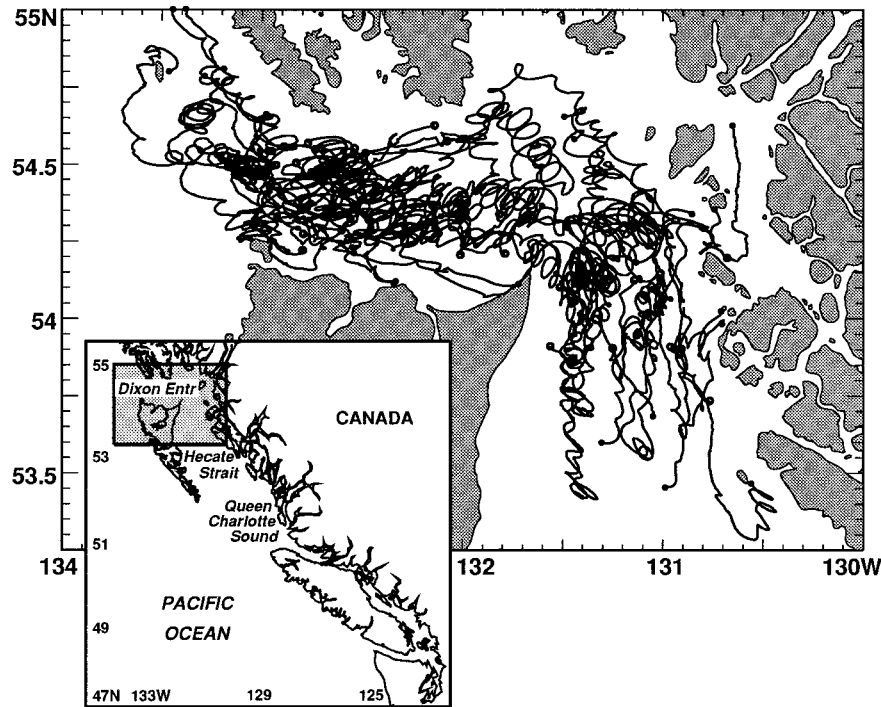


FIG. 1. Loran C drifter tracks in Dixon Entrance and in northern Hecate Strait (shaded area in inset), along the north coast of British Columbia, in the summer of 1991.

Model velocities were computed at the hourly drifter positions using the eight largest tidal constituents for the region—K1, O1, P1, Q1, M2, S2, N2, K2—interpolated from nearby model nodal points, as is described below. For this particular study, we applied the surface constituent values calculated by the three-dimensional, barotropic, finite element model of Ballantyne et al. (1996). In order to match the drifter record, each data point in the model time series matches the time and position of the drifter series; however, model velocities were instantaneous values, whereas observed drifter velocities were essentially 1-h averages. This averaging reduces the observed semidiurnal speeds by 1%, and diurnal and inertial speeds by a smaller amount.

Each of the drifter and model velocity time series were divided into equal segments of fixed duration, chosen from Table 1. For reasons discussed below, a 74-h segment was used in most analyses. When required, we also used segment durations ranging from 1 to 6 days. A linear trend was removed from each drifter velocity segment by fitting straight lines to upper and lower wave envelopes and taking their mean value. This type of detrending is preferable to fitting a straight line to all data points because for short-duration wavelike signals a single line would be dependent on the relative phases of the waves. Model velocity segments required no detrending.

For most spectral analysis applications, the use of

TABLE 1. Candidate durations (integral hours) for velocity segments and spectral bands they may approximately fit (D: diurnal, I: inertial, SD: semidiurnal). The numbers in columns D and SD are the ratios between each segment duration and average band “periods” (see text), 24.666 h for D and 12.337 for SD bands. The ratio for the inertial period (I) depends on latitude. Two periods used here are 15.4 and 14.8 h, for 51° and 54°N, respectively. The last column gives our qualitative assessment of each entry.

Duration (h)	D	I <sub>51</sub>	I <sub>54</sub>	SD	Comments
24	0.973	1.56	1.62	1.945	Only for D and SD
25	1.014	1.62	1.69	2.026	Only for D and SD
37	1.500	2.40	2.50	2.999	Only for SD
48	1.946	3.11	3.24	3.891	A reasonable choice
49	1.986	3.18	3.31	3.972	A reasonable choice
62	2.513	4.02	4.19	5.026	Only for I and SD
74	3.000	4.81	5.00	5.998	A better choice
87	3.527	5.65	5.88	7.052	Only for I and SD
98	3.973	6.36	6.62	7.944	Only for D and SD

TABLE 2. Model tidal velocity constituents, their frequency (cpd), major and minor semiaxis amplitudes (cm s<sup>-1</sup>), and tidal ellipse angle of inclination ( $\theta$ ) near 51.7°N, 129.2°W. The symbols  $a^-$  and  $a^+$  are clockwise and counterclockwise rotary velocity amplitudes, respectively.

Name	Frequency	$a^+ + a^-$	$a^+ - a^-$	$\theta$
Q1	0.898	1.129	-0.961	10.1
O1	0.930	7.464	-6.419	11.0
P1	0.997	3.588	-3.081	15.6
K1	1.003	11.605	-10.118	16.5
N2	1.896	6.769	-4.263	55.9
M2	1.932	33.395	-21.131	57.9
S2	2.000	10.372	-5.882	58.2
K2	2.005	2.987	-1.853	58.1

tapered windows is recommended to reduce the influence of sharp transitions in signal level between the ends of the records. Such techniques assume broadband shapes across the spectrum. However, tidal signals are composed of many line spectra, which may be broadened slightly by oceanic influences or by the nonstationarity of the record but are by no means broadband in nature. The effect of tapering such signals is to reduce the sidelobes. However, tapering also broadens the peaks of individual tidal lines and thus reduces spectral resolution, which is especially detrimental when using short-duration signals. A reasonable alternative to tapering is to select segments whose durations are integral multiples of periods of main tidal constituents.

Table 1 lists possible choices of segment durations that are less than 100 h and the ratios among these durations and those of the dominant bands: diurnal  $T_D$ , inertial  $T_I$ , and semidiurnal  $T_{SD}$ . The nominal frequen-

cies of diurnal (D) and semidiurnal (SD) bands,  $f_D$  and  $f_{SD}$ , are estimated as averages of the four dominant constituent frequencies in each band, using model-calculated major-axis amplitudes of constituent current ellipses as weights (an example is given in Table 2). This calculation gives average periods for our area of study,  $T_D = 24.666$  and  $T_{SD} = 12.337$  h, with corresponding standard deviations of 0.073 and 0.002 h, respectively. The much larger standard deviation for the diurnal period is likely due to existence of diurnal coastal trapped waves in the model.

The inertial (I) band ratios in Table 1 are calculated for two latitudes within our region: 51° and 54°N. Although we apply this analysis to the Northern Hemisphere, it is equally valid for regions south of the equator, where the sense of rotation of the dominant signal is reversed.

Six of the 10 entries in Table 1 are suitable for pro-

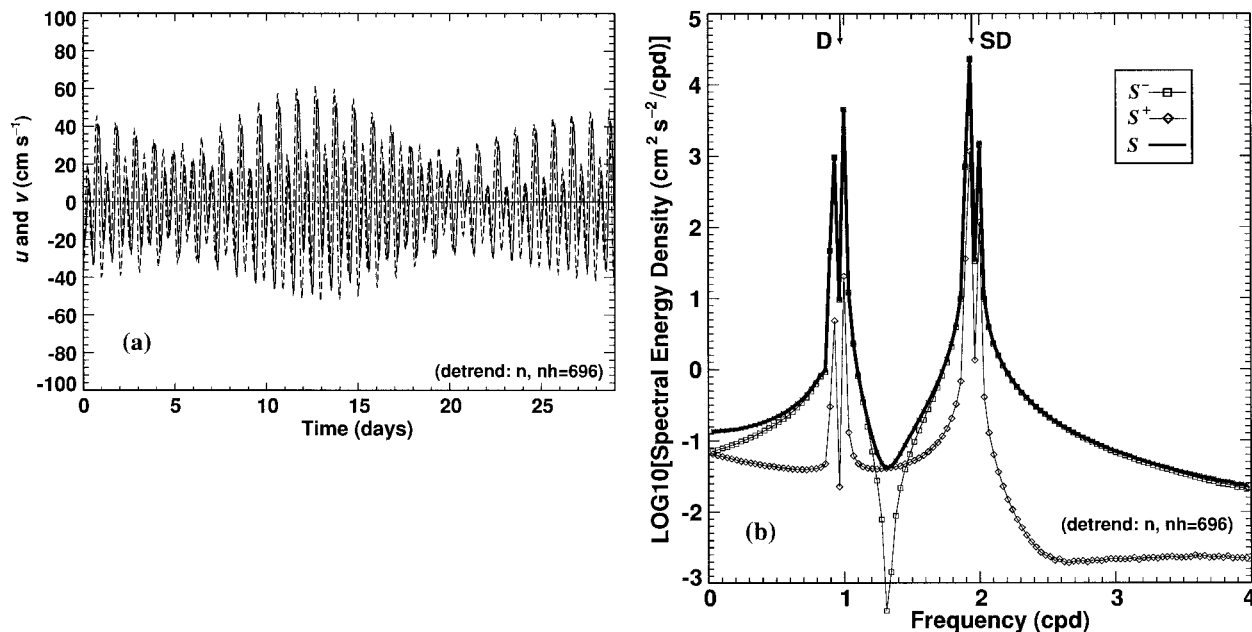


FIG. 2. (a) Horizontal velocity components  $u$  (solid) and  $v$  (dashed) during a 29-day spring-neap cycle near 51.7°N, 129.2°W, as produced by a tidal model of the north coast of British Columbia (Ballantyne et al. 1996). (b) Logarithm of spectral energy density: total ( $S$ , thick line), clockwise ( $S^-$ , squares), and counterclockwise ( $S^+$ , diamonds). The four peaks in (b) are from tidal constituents O1 + Q1, K1 + P1, M2 + N2, and S2 + K2. The two arrows along the top axis mark diurnal (D) and semidiurnal (SD) band “frequencies,” averaged from each band constituent frequencies, using as weights their major semiaxis amplitudes.

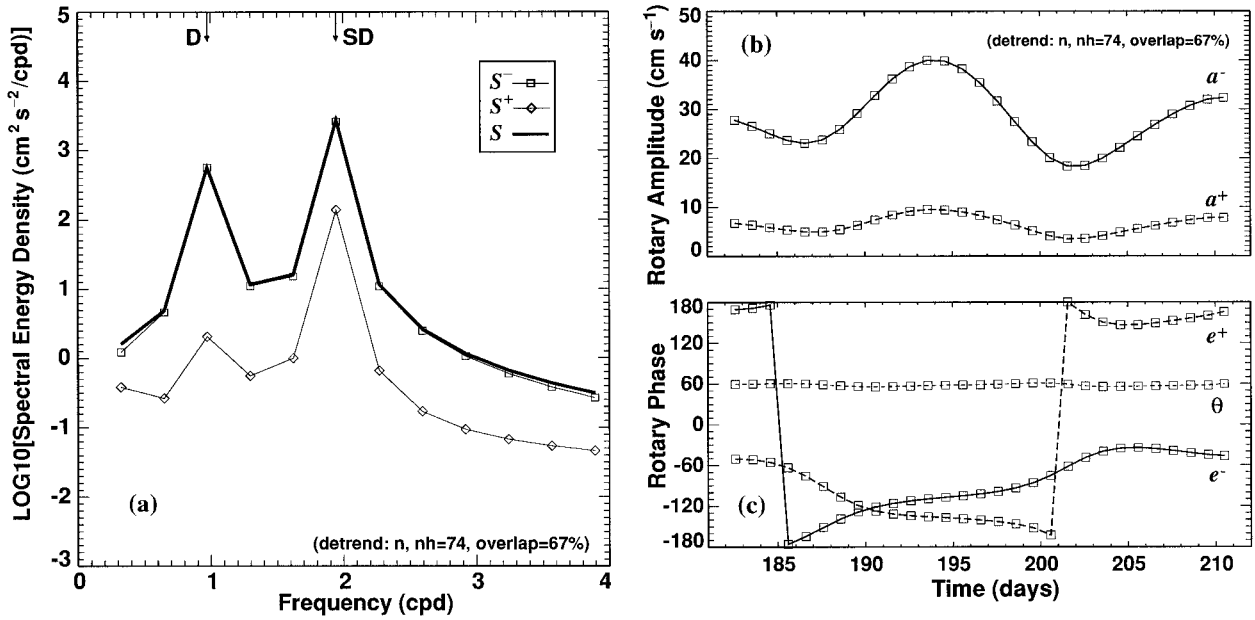


FIG. 3. (a) As in Fig. 2b but averaged from 29 consecutive 74-h segments with 67% overlap. (b) Clockwise ( $a^-$ , solid lines) and counterclockwise ( $a^+$ , dashed) rotary vector amplitudes. (c) Clockwise ( $e^-$ , solid) and counterclockwise ( $e^+$ , dashed) rotary vector phases (referenced to midpoint of the time series). The values in (b) and (c) were calculated from complex FFT amplitudes at  $f_6 = 6/74 \text{ cph} = 1.9459 \text{ cpd}$ , during days 182–212 in 1995. This frequency is very close, though not identical, to our estimate of the SD band frequency,  $f_{SD} = 1.9447 \text{ cpd}$ . The sum (difference) of the two curves in (a) gives the major (minor) semiaxis of the tidal ellipse, while the short-dashed line in (c) shows its angle of inclination ( $\theta$ ), as computed from (6).

cessing of D and SD bands, but only 3 of these, 48, 49, and 74 h, also have a spectral line near the I band. Of these three, we selected the 74-h duration as a better choice because its D and SD band ratios are nearly integral, while the I band ratio approaches 5 in most of the area. We thus expect less leakage between the three bands when calculating fast Fourier transforms (FFTs) from 74-h segments.

Spectral energy density and rotary velocity spectra (Gonella 1972; Mooers 1973) were computed from FFTs of Cartesian velocity components  $u$  and  $v$ . Rotary velocity clockwise and counterclockwise spectral amplitudes,  $a^-$  and  $a^+$ , and phases,  $e^-$  and  $e^+$ , were calculated at each frequency, as in Foreman (1978):

$$a^- = 1/2[(CX - SY)^2 + (CY + SX)^2]^{1/2}, \quad (1)$$

$$a^+ = 1/2[(CX + SY)^2 + (CY - SX)^2]^{1/2}, \quad (2)$$

$$e^- = \arctan[(CY + SX)/(CX - SY)], \quad (3)$$

$$e^+ = \arctan[(CY - SX)/(CX + SY)], \quad (4)$$

where

$$(CX, CY, SX, SY) = (X \cos \phi_x, Y \cos \phi_y, X \sin \phi_x, Y \sin \phi_y), \quad (5)$$

and  $(X, \phi_x)$  and  $(Y, \phi_y)$  are spectral line amplitudes and phases from the FFTs of  $u$  and  $v$ , respectively.

Phase values,  $\phi_x$  and  $\phi_y$ , of successive velocity segments are reduced to a common time origin  $t_0$ , chosen to be in the middle of the complete time series, which

reduces phase progression through the record. Nevertheless, we use phase *differences* between model and observed tidal spectra when interpreting the results and comparing with models.

For the discussion here, it is sufficient to compute the rotary amplitudes,  $a^+$  and  $a^-$ , and the phases,  $e^+$  and  $e^-$ . The major and minor semiaxes of the tidal velocity ellipse are  $(a^+ \pm a^-)$ . Hence, a negative (positive) minor semiaxis denotes clockwise (counterclockwise) rotation of the velocity vector. Angle of inclination of the ellipse is

$$\theta = \frac{1}{2}(e^+ + e^-) \pmod{180^\circ}. \quad (6)$$

### 3. Eulerian examples

Examples in this section are derived from ocean surface, tidal velocity time series at a fixed location. These were constructed from four diurnal and four semidiurnal constituent amplitudes and phases (Table 2), as calculated by a barotropic, three-dimensional, finite element model for the north coast of British Columbia (Ballantyne et al. 1996). Since individual amplitudes and phases of these constituents do not change over the duration of the record, this example provides a test of the ability of our analysis of short segments to track the spring-neap cycle and to maintain stable phases. As these are pure waves at a fixed location, no detrending is required.

Figure 2a shows model tidal velocity components

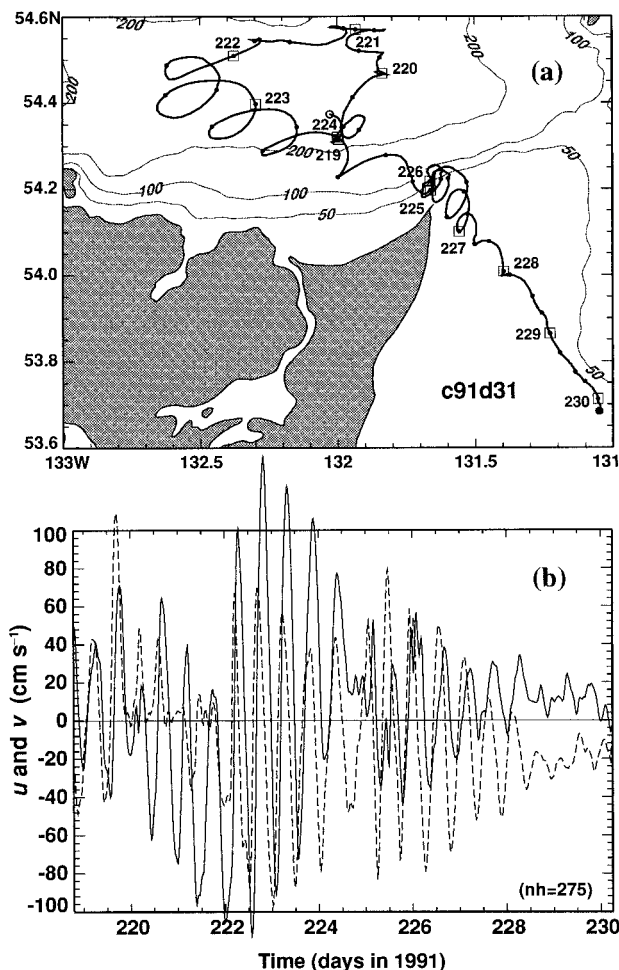


FIG. 4. (a) Loran C drifter track c91d31 in Dixon Entrance and Hecate Strait, 7–19 August 1991 (hollow and solid circles show start and end of the track; dots and squares mark 6-h positions and locations at 2400 UTC, with elapsed days in 1991 given near each square; bathymetric contours, in meters, are from the finite element tidal model). (b) Drifter  $u$  (solid line) and  $v$  (dashed) velocity components.

during a 29-day period at node 3742 (near 51.7°N, 129.2°W). The logarithm of spectral energy density ( $S$ ) of this velocity time series is plotted in Fig. 2b. No spectral smoothing has been applied to these line spectra. Therefore, each plotted value has only 2 degrees of freedom and large confidence limits. On the other hand, noise level in this figure is four to five orders of magnitude less than the spectral peak values.

Two distinct peaks are observed in each of the D and SD bands in Fig. 2b, although we do not attempt to resolve the four individual constituents in each band. For example, we do not resolve each of the N2 and M2 signals in the largest peak in Fig. 2b. At this location, model tidal energy is almost entirely due to the clockwise rotary component ( $S^-$ ). The counterclockwise component ( $S^+$ ) is smaller by about one (two) order of magnitude in the SD (D) band.

The same velocity time series was split into 29 seg-

ments, each of 74-h duration, with 67% overlap, or about one segment per day. Figure 3a shows the logarithm of the average spectral density  $S$  and of its rotary components,  $S^-$  and  $S^+$ , computed from these 29 segments. As in Fig. 2b, the counterclockwise component is weaker than the clockwise by about one (two) order(s) of magnitude for the SD (D) band. The consecutive rotary vector amplitudes and phases of the SD band are shown in Figs. 3b and 3c, respectively. The spring-neap cycle is clearly shown in Fig. 3b, both in clockwise and counterclockwise amplitude plots. The velocity semimajor axis (the sum of the two curves in Fig. 3b) varies between 28 and 50  $\text{cm s}^{-1}$ . This fortnightly variation is mainly due to beating between M2 and S2 tidal constituents, as shown in this figure, because the four semidiurnal constituents are represented by one frequency bin in the spectrum.

Rotary phase plots in Fig. 3c show opposite changes for the two rotary components during the spring-neap cycle. Uncertainty and changes in  $f_{SD}$  due to varying contributions from band constituents add to the apparent phase changes in Fig. 3c. Given this drift in phases, we compare relative phase values between the spectra of model and drifters.

The mean value of the angle of inclination  $\theta$ , as computed from (6) (short-dashed line in Fig. 3c), and its standard deviation are 58.04° and 1.75°, respectively. This agrees quite well with the four SD  $\theta$  values in Table 2 due to an almost complete cancellation in (6) of the rotary components phase drift.

Experiments with shorter segments of 49- and 25-h duration show reasonable results, although when drifter data contain inertial oscillations, these shorter segments are not appropriate. To summarize this section, the 74-h segments were found to be adequate for getting rotary velocity amplitudes and tidal ellipse angles of inclination for dominant frequency bands. Shorter segment durations, for example, 49 or 25 h, can be used to enhance spatial and temporal resolution if there is little inertial-period energy between the two main tidal bands.

#### 4. Lagrangian examples

We now shift attention to rotary spectra calculated from velocities of a Loran C drifter. We compare these to spectra of velocities from the tidal model, which are obtained as follows. For each half-hourly drifter position, we first calculate coefficients in (5) (sine and cosine amplitudes of east and north components of velocity) using model amplitudes and phases at the three nearest nodes. These coefficients are linearly interpolated to the drifter location and are converted back to amplitudes and phases, giving contributions to model velocity, at drifter time and position, from each of the eight constituents in Table 2. Finally, these are summed to give model tidal velocities along the drifter track.

This repeated transformation between (amplitude, phase) and (sine, cosine) formats is required to maintain

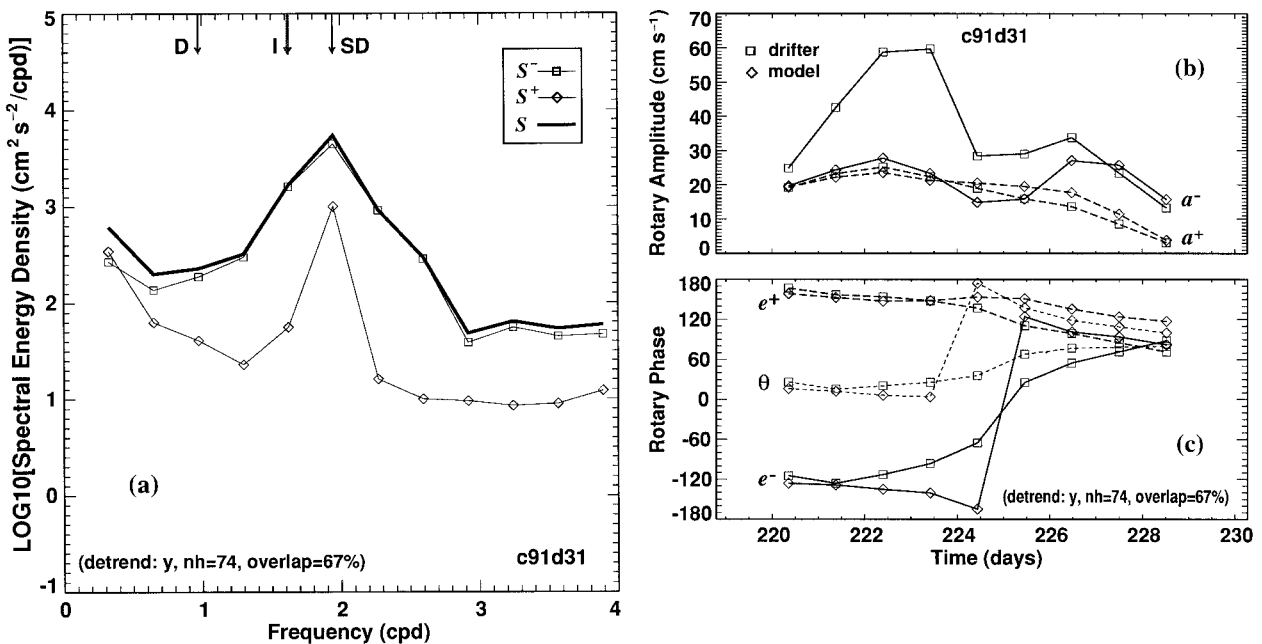


FIG. 5. (a) Logarithm of mean spectral energy density ( $S$ ) from drifter track c91d31, averaged from 11 74-h segments, with 67% overlap; total (thick line), clockwise ( $S^-$ , squares), and counterclockwise ( $S^+$ , diamonds). Additional arrow (compared to Fig. 3a) shows the inertial (I) band frequency range, calculated at a central latitude in each segment. (b) Amplitudes ( $a^\pm$ ), (c) phases ( $e^\pm$ ), and angles of inclination ( $\theta$ ) of the semidiurnal tidal ellipse (clockwise: solid line, counterclockwise: dashed, angle of inclination: short dashed; squares and diamonds mark drifter and model values, respectively).

consistency with the model calculations, as the finite element model assumes that CX, SX, CY, SY vary linearly over each triangle of the finite element grid. Thus, a linear interpolation of these coefficients is appropriate, while linear interpolation of amplitudes and phases, or of total velocities, is not consistent. However, tidal model results are usually stored as amplitudes and phases of each constituent at each node.

#### a. Example 1: Strong internal semidiurnal tides

Figures 4a and 4b show an example of Loran C drifter track c91d31 (deployed in the summer of 1991) and its velocity components. It was selected from about 200 tracks of Loran C drifters deployed along the north coast of British Columbia between 1990 and 1995. A more complete description of these data is given in Crawford et al. 1998.

The semidiurnal (SD) energy dominates the c91d31 velocity spectra (Fig. 5a), computed from overlapping (by 67%) 74-h segments. This drifter motion is mainly clockwise rotary, as is also inferred from its rotary coefficient value,  $r = (S^- - S^+) / (S^- + S^+)$ , which is near unity for all three bands. Along-track SD rotary amplitudes, rotary phases, and ellipse angles of inclination are shown in Figs. 5b,c, together with corresponding values from the tidal model.

The counterclockwise amplitudes and phases agree between this drifter and the model almost everywhere, but the drifter clockwise amplitudes are much higher in

Dixon Entrance. The clockwise phases and angles of inclination shift significantly as the drifter moves from Dixon Entrance into northern Hecate Strait on day 225. The two graphs of contours of the logarithm of rotary energy density, presented in Figs. 6a,b, also reveal a rapid shift near day 225, particularly in the clockwise components. Obviously, there is a change in the nature of tidal currents between Hecate Strait and Dixon Entrance.

We suspect this shift may be more rapid than portrayed by Figs. 5 and 6, which present averages over 74 h, and that the use of shorter segments would reveal a more abrupt transition. We noted earlier that 25-h segments are also suitable for investigating tidal currents, although this interval may include inertial velocities together with the tidal velocities. We therefore first examined higher-resolution spectra from two 148-h segments (with 14% overlap). These showed more than an order of magnitude less spectral energy density at  $f_1 = 1.62$  cpd (counts per day) than at  $f_{SD}$ . Therefore, calculations over 25-h segments are valid representations of tidal motion for this track with insignificant contributions from inertial currents.

Figures 7a and 7b show rotary amplitudes and phases when using 25-h segments with 50% overlap. These are similar to Figs. 5b,c, respectively, except that 25-h segments better resolve occurrences of extreme amplitudes (note the difference in vertical scales between Figs. 5b and 7a) and rapid phase changes at day 225. Shorter segments also allow extension of these figures closer to

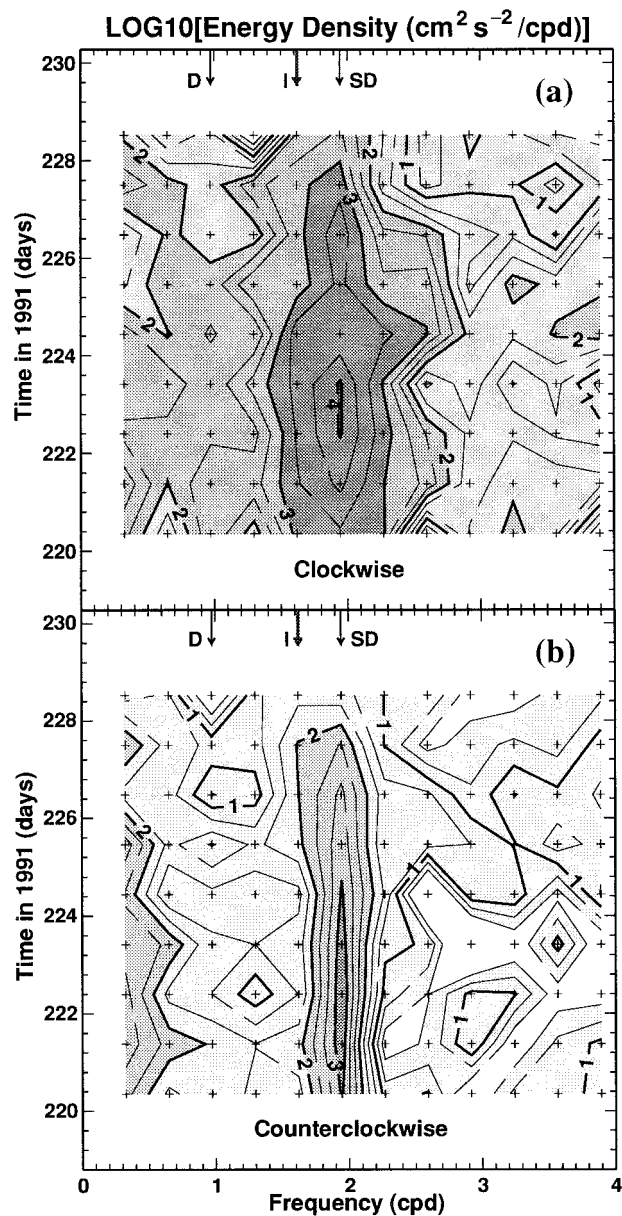


FIG. 6. Contours of a logarithm of (a) clockwise and (b) counterclockwise spectral energy density for drifter track c91d31, as a function of time and frequency, from same velocity segments as in Fig. 5 (only positive contours are shown; the “+” symbols show the data points; arrows along the top axis mark “frequencies” of D, I, and SD bands).

the ends of the track, thereby revealing additional details that were not seen in Figs. 5b,c. For example, the counterclockwise amplitudes in Fig. 7a drop toward the noise level of about  $1 \text{ cm s}^{-1}$  after day 228, rendering the counterclockwise phase and angle of inclination values in Fig. 7b meaningless during that time. However, the clockwise phase lags provided by the model are comparable to the drifter values, indicating that the model can replicate the actual tidal currents well in regions where internal tides are weak.

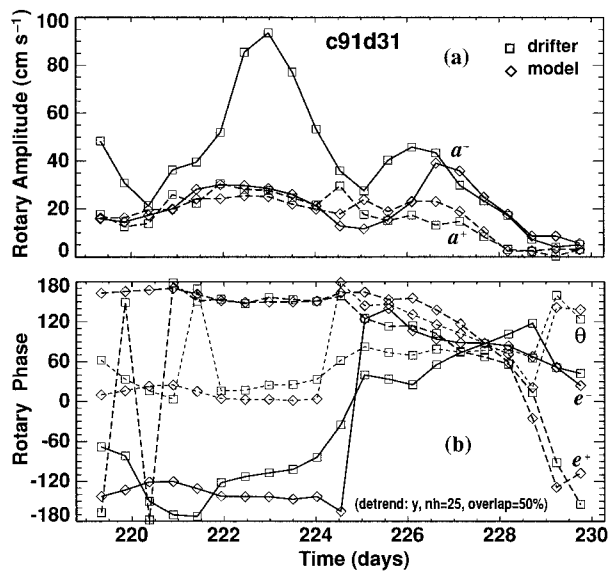


FIG. 7. (a) and (b) As in Figs. 5b and 5c but from 25-h segments with 50% overlap.

Figures 8a and 8b show clockwise and counterclockwise SD amplitudes from all 74-h segments of Loran C tracks in Dixon Entrance and in northern Hecate Strait during July and August 1991, as well as their differences from amplitudes calculated in the model. Overall, the agreement between near-surface drifter and model velocities is much better in Hecate Strait than in Dixon Entrance. The intensified clockwise SD motion in Dixon Entrance is attributed mainly to internal tides with strong clockwise (in the Northern Hemisphere) components of velocity, which are usually generated by vertical motion of isopycnals at nearby topographic slopes. Such internal-wave-type motion cannot be represented by a barotropic tidal model, hence the discrepancy between drifter and model currents. In nearby Hecate Strait the waters are shallow and well mixed along the northeastern shore, and internal tides are suppressed almost completely. In this region the barotropic model and drifter observations agree more closely.

The anomalous region at the western end of Dixon Entrance, where model speeds actually exceed observed speeds, lies over a shallow region called Learmonth Bank (near  $54.5^\circ\text{N}$ ,  $133^\circ\text{W}$ ; Fig. 8). This anomaly emerges clearly in the counterclockwise components (Fig. 8b), indicating a local change in the dynamics of the tidal flow.

*b. Example 2: Comparable inertial and semidiurnal currents*

In Queen Charlotte Sound, about 300 km south of Dixon Entrance (Fig. 1), tidal currents are weaker, and significant inertial oscillations have been reported (Thomson and Huggett 1981; Kundu and Thomson 1985). About 10% of our Loran C drifter tracks have

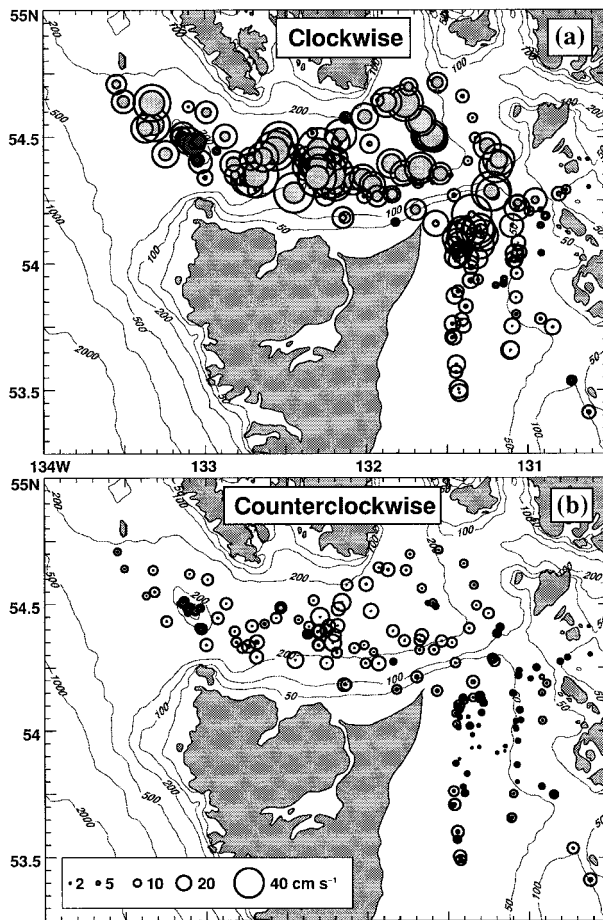


FIG. 8. Semidiurnal (a) clockwise ( $a^-$ ) and (b) counterclockwise ( $a^+$ ) rotary velocity amplitudes from overlapping 74-h segments of Loran C drifter tracks in Dixon Entrance and in northern Hecate Strait during 1 July–19 August 1991 (Fig. 1). The diameter of outer circles is proportional to the amplitude, while the diameter of inner filled circles is proportional to drifter–model amplitude difference. A darker fill shade is used for negative difference values (larger model amplitudes).

spectral energy levels in the I band comparable to those of the SD band, whereas the remaining 90% have much less energy in the I band. This is in contrast to more dominant energy in the I band that is observed in deep ocean drifters of the northeast Pacific (Thomson et al. 1998).

Figure 9 displays the drifter track c90a21, passing through northern Queen Charlotte Sound and southern Hecate Strait during a period of pulsing northwesterly winds. Most of this track lies more than 50 km from shore, over waters more than 200 m deep, where tidal currents are about  $10 \text{ cm s}^{-1}$  or less. We therefore expect significant inertial signals.

Figures 10a and 10b show the time series of clockwise and counterclockwise energy density spectra from overlapping 74-h segments (cf. Figs. 6a,b). In the I band (adjacent to the SD band) these figures reveal the classic inertial oscillation pattern of strong clockwise compo-

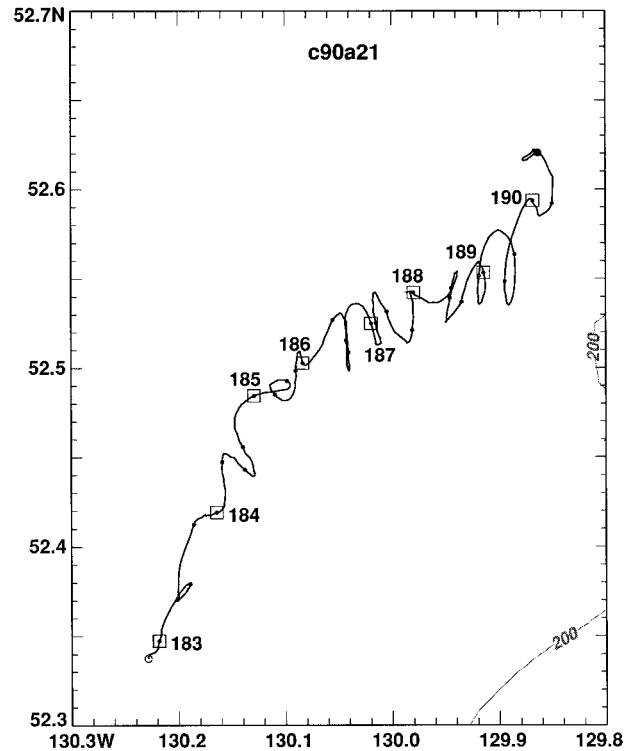


FIG. 9. Loran C drifter track c90a21, passing from northern Queen Charlotte Sound into southern Hecate Strait, 11–18 August 1990 (hollow and solid circles show start and end of the track; dots and squares mark the 6-h positions and locations at 2400 UTC, with elapsed days in 1990 given near each square; this part of the shelf is 200–300 m deep).

nents (Fig. 10a) and weak counterclockwise components (Fig. 10b), corresponding to a rotary coefficient value of  $r(f_1) \approx 1$ . These spectra have a minimal separation between SD and I bands, but a repeat with 148-h segments (Fig. 10c) shows there is indeed a spectral gap between these two bands and that the 74-h segment duration provides sufficient separation.

## 5. Discussion and conclusions

Over the past decade we have accumulated over 200 data records of the tracks of Loran C surface drifters in the coastal waters of western Canada and about 60% of these tracks are longer than 73 h. We expect that other oceanographic labs have similar records for their nearby coastal zones. Our goal here is to develop a spectral technique to evaluate the output of a numerical tidal model in coastal waters using our drifter data. Although such data are often difficult to interpret, there are several advantages to this approach in areas where spatial gradients are large and nontidal flows are relatively weak.

- 1) With present technology, the cost of drifters is low compared to the cost of moored currents meters, and the cost of deployment of drifters can be very low if ships of opportunity are used.

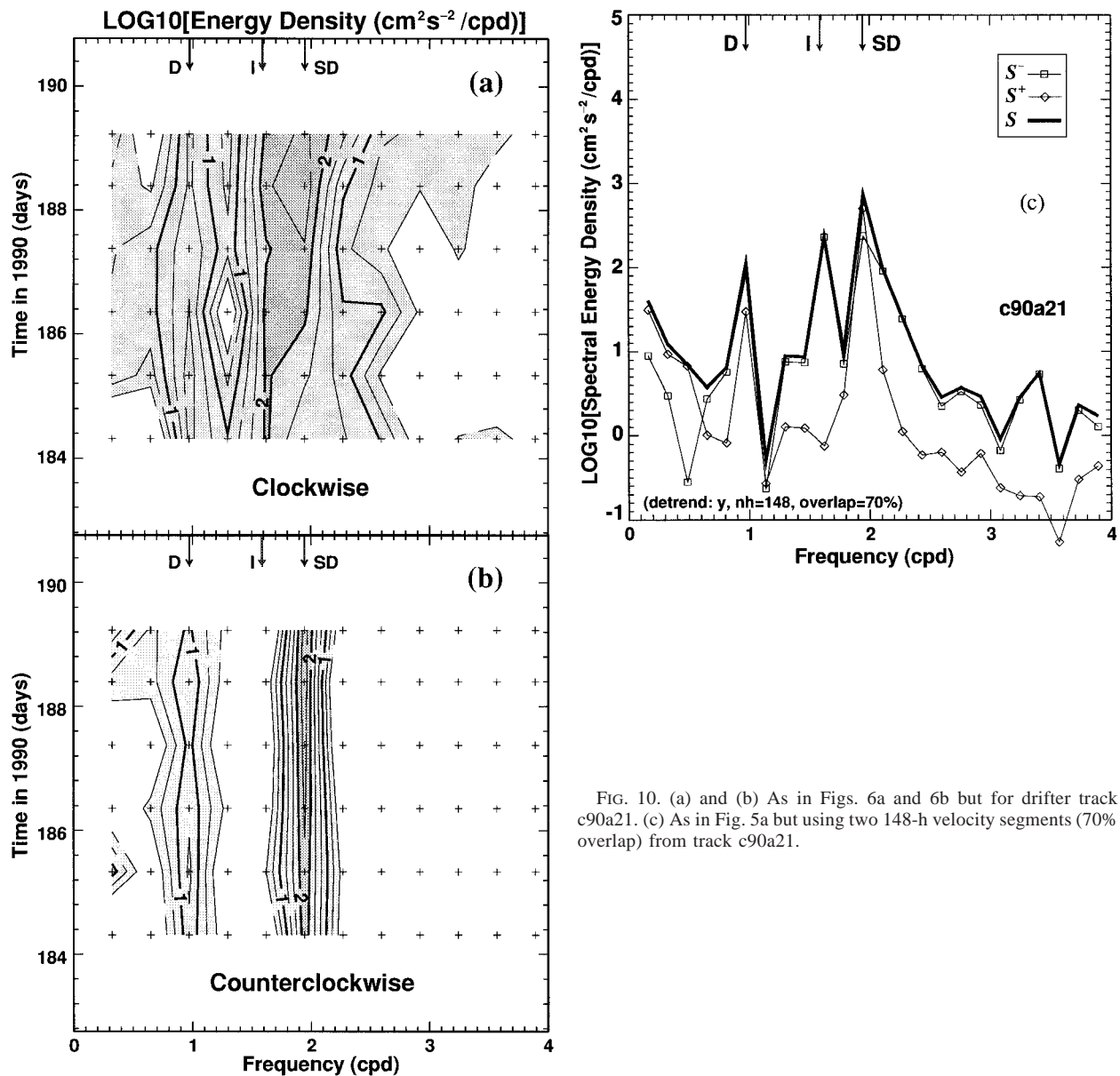


FIG. 10. (a) and (b) As in Figs. 6a and 6b but for drifter track c90a21. (c) As in Fig. 5a but using two 148-h velocity segments (70% overlap) from track c90a21.

- 2) The most recent drifters supplied to us are small and rugged. Conventional current meter moorings, on the other hand, require large surface floats, which may block shipping channels and are vulnerable to collisions.
- 3) A drifter can cover a broad region of the continental shelf, providing short segments of observations along the way. The drifter tracks can define eddies and trace out the path of oil spills or fish larvae, thus providing a variety of useful information. On the other hand, current meter moorings provide excellent temporal information but poor spatial coverage.

To improve the interpretation of drifter data, we compare model and drifter velocities at identical positions

and times along each track, and although the statistical significance of any one comparison is low, repeated sampling along successive drifter tracks improves the comparison. As an example, the model/drifter comparisons for northern Hecate Strait and Dixon Entrance along the Pacific coast of Canada show the transition from a region of strong internal tides to one of virtually no internal tides.

Our comparison shows that a barotropic tidal model of SD currents is inadequate in some regions. It also provides excellent evaluation data for new baroclinic models that are capable of resolving internal tides. By using rotary spectra, we separate diurnal and semidiurnal rotary tidal currents and isolate the mainly circular

inertial motions. We have applied this technique to Loran C drifters, which report positions at half-hour intervals. But it could also be applied to Argos drifter data that are available at longer and less regular intervals.

*Acknowledgments.* All support for this project and for drifter tracking was provided by Fisheries and Oceans Canada and by the Panel for Energy Research and Development, Project 6B2003. Drifter deployments were undertaken by Axys Environmental Consulting and by the Canadian Hydrographic Service, under the direction of M. J. Woodward. B. de Lange Boom and R. E. Thomson provided helpful comments on the manuscript.

#### REFERENCES

- Ballantyne, V. A., M. G. G. Foreman, W. R. Crawford, and R. Jacques, 1996: Three-dimensional model simulations for north coast of British Columbia. *Cont. Shelf Res.*, **16**, 1655–1682.
- Crawford, W. R., 1988: The use of Loran-C drifters to locate eddies on the continental shelf. *J. Atmos. Oceanic Technol.*, **5**, 671–676.
- , M. J. Woodward, M. G. G. Foreman, and R. E. Thomson, 1995: Oceanographic features of Hecate Strait and Queen Charlotte Sound in summer. *Atmos.-Ocean*, **33**, 639–681.
- , J. Y. Cherniawsky, P. F. Cummins, and M. G. G. Foreman, 1998: Variability of tidal currents in a wide strait: A comparison between drifter observations and numerical solutions. *J. Geophys. Res.*, in press.
- Cummins, P. F., and L. Y. Oey, 1997: Simulation of barotropic and baroclinic tides off northern British Columbia. *J. Phys. Oceanogr.*, **27**, 762–781.
- Foreman, M. G. G., 1978: Manual for tidal currents analysis and prediction. Pacific Mar. Sci. Rep. 78–6, 70 pp. [Available from Inst. of Ocean Sci., P. O. Box 6000, Sidney, BC V8L 4B2, Canada.]
- , R. F. Henry, R. A. Walters, and A. V. Ballantyne, 1993: A finite element model for tides and resonance along the north coast of British Columbia. *J. Geophys. Res.*, **98**, 2509–2531.
- Gonella, J., 1972: A rotary-component method for analyzing meteorological and oceanographic vector time series. *Deep-Sea Res.*, **19**, 833–846.
- Kundu, P. K., and R. E. Thomson, 1985: Inertial oscillations due to a moving front. *J. Phys. Oceanogr.*, **15**, 1076–1084.
- Mooers, C. N. K., 1973: A technique for the cross spectrum analysis of pairs of complex-valued time series, with emphasis on properties of polarized components and rotational invariants. *Deep-Sea Res.*, **20**, 1129–1141.
- Thomson, R. E., and W. S. Huggert, 1981: Wind-driven inertial oscillations of large spatial coherence. *Atmos.-Ocean*, **19**, 281–306.
- , P. H. LeBlond, and A. B. Rabinovich, 1997: Oceanic odyssey of a satellite-tracked drifter: North Pacific variability delineated by a single drifter trajectory. *J. Oceanogr.*, **53**, 81–87.
- , —, —, 1998: Satellite-tracked drifter measurement of inertial and semidiurnal currents in the northeast Pacific. *J. Geophys. Res.*, in press.
- Woodward, M. J., W. R. Crawford, K. F. Drinkwater, and M. J. Hill, 1991: Lagrangian measurements of surface currents using Loran-C drifters. *Proc., Oceans '91*, IEEE, 1190–1196.